

High-Voltage Oxygen-Redox-Based Cathode for Rechargeable Sodium-Ion Batteries

Aishuak Konarov, Hee Jae Kim, Jae-Hyeon Jo, Natalia Voronina, Yongseok Lee, Zhumabay Bakenov, Jongsoo Kim,* and Seung-Taek Myung*

Recently, anionic-redox-based materials have shown promising electrochemical performance as cathode materials for sodium-ion batteries. However, one of the limiting factors in the development of oxygen-redox-based electrodes is their low operating voltage. In this study, the operating voltage of oxygen-redox-based electrodes is raised by incorporating nickel into P2-type $\text{Na}_{2/3}[\text{Zn}_{0.3}\text{Mn}_{0.7}]\text{O}_2$ in such a way that the zinc is partially substituted by nickel. As designed, the resulting P2-type $\text{Na}_{2/3}[(\text{Ni}_{0.5}\text{Zn}_{0.5})_{0.3}\text{Mn}_{0.7}]\text{O}_2$ electrode exhibits an average operating voltage of 3.5 V and retains 95% of its initial capacity after 200 cycles in the voltage range of 2.3–4.6 V at 0.1C (26 mA g⁻¹). Operando X-ray diffraction analysis reveals the reversible phase transition: P2 to OP4 phase on charge and recovery to the P2 phase on discharge. Moreover, ex situ X-ray absorption near edge structure and X-ray photoelectron spectroscopy studies reveal that the capacity is generated by the combination of $\text{Ni}^{2+}/\text{Ni}^{4+}$ and $\text{O}^{2-}/\text{O}^{1-}$ redox pairs, which is supported by first-principles calculations. It is thought that this kind of high voltage redox species combined with oxygen redox could be an interesting approach to further increase energy density of cathode materials for not only sodium-based rechargeable batteries, but other alkali-ion battery systems.

1. Introduction

Oxygen redox has become an emerging topic for rechargeable battery systems employing monovalent charge carriers such as lithium or sodium.^[1–3] To meet the increasing demands of the various applications of lithium-ion batteries (LIBs), their energy density must be further increased. Recent concerns associated with the fluctuation in price of LIBs resulting from limited lithium resources are considered as emerging opportunities to extend research interest toward sodium-ion batteries

Dr. A. Konarov, H. J. Kim, J.-H. Jo, N. Voronina, Y. Lee, Prof. J. Kim, Prof. S.-T. Myung
Department of Nano Technology and Advanced Materials Engineering
Sejong University
Gunja-dong, Gwangjin-gu, Seoul 05006, South Korea
E-mail: jongsookim@sejong.ac.kr; smyung@sejong.ac.kr

Dr. A. Konarov, Prof. Z. Bakenov
National Laboratory Astana
Nazarbayev University
Institute of Batteries LLC
53 Kabanbay Ave, Nur-Sultan 010000, Kazakhstan

 The ORCID identification number(s) for the author(s) of this article can be found under <https://doi.org/10.1002/aenm.202001111>.

DOI: 10.1002/aenm.202001111

(SIBs), for which the reaction chemistries are similar to those of LIBs.^[4–8] To reach similar energy densities as LIBs, promising cathode materials for SIBs must possess high capacity to compensate for their intrinsically low operation voltages. As the capacities of cathode materials can reach their limit when using transition metal redox, it is anticipated that redox of oxygen in the crystal structure can contribute additional capacity and boost the resulting energy density.^[9,10] Representative works were performed in the early 2000s, specifically, on Li_2MnO_3 ($\text{Li}[\text{Li}_{1/3}\text{Mn}_{2/3}]\text{O}_2$) layered material,^[11,12] which has the same crystal structure as typical LiTMO_2 (TM = transition metal). Li_2MnO_3 is electrochemically inactive because $\text{Mn}^{4+}/\text{Mn}^{5+}$ redox is not available within the normal cutoff voltage window. However, the material delivered a capacity beyond the theoretical limit attributed to the transition metal redox (300 mAh g⁻¹).^[12] Earlier works suggested that the delivered capacity could

be attributed to oxygen loss from the oxide lattice;^[12] however, state-of-the-art characterization later proved that the main contributor to the capacity was associated with the oxygen redox,^[13] which triggered the intensive study of oxygen redox. Recently, there are some arguments to verify the chemical state of lattice oxygen during electrochemical reaction. Earlier work by Tarascon et al.^[9] demonstrated the oxygen activity using X-ray photoelectron spectroscopy (XPS), X-ray absorption spectroscopy (XAS), and electron paramagnetic resonance (EPR) in $\text{Li}_2\text{Ru}_{1-y}\text{Sn}_y\text{O}_3$ compound. In situ or operando Raman spectroscopy and surface-enhanced Raman spectroscopy (SERS) become important tools in identifying the formation of peroxo-like species (O_2^{n-}).^[14,15] Yang and Devereaux^[16] highlighted the importance of using resonant inelastic X-ray scattering (RIXS) to identify the activity of lattice oxygen in oxide materials. From the above facts, it is considered that combination of the above-mentioned characterization tools with theoretical thermodynamic prediction may provide more reliable results to understand the oxygen redox chemistry.

The oxygen redox reaction has also been extensively investigated in SIBs to achieve additional capacity.^[17–19] For SIBs, Na_2MnO_3 ($\text{Na}[\text{Na}_{1/3}\text{Mn}_{2/3}]\text{O}_2$), which has the same crystal structure as Li_2MnO_3 , has also been considered despite the large difference in the ionic size between sodium and manganese. For

instance, Yabuuchi et al.^[20] demonstrated the stabilization of sodium in the transition metal layer with lithium with the form of a P2-type $\text{Na}_{5/6}[\text{Li}_{1/4}\text{Mn}_{3/4}]\text{O}_2$ compound. The compound showed a similar voltage profile as that observed for a Li_2MnO_3 -based composite. However, although the composite delivered a high discharge capacity of 200 mAh g^{-1} , further improvement of the cycling performance was required. They also proposed P2-type $\text{Na}_{2/3}[\text{Mn}_{0.72}\text{Mg}_{0.28}]\text{O}_2$,^[21] for which the long plateau appearing on charge is the result of oxygen redox, because the oxidation state of Mn cannot vary over 4+ in the operation window (1–5 V). Later, Maitra et al.^[22] confirmed the availability of oxygen redox in the compound. Recently, we suggested the occurrence of an oxygen redox reaction in P2- $\text{Na}_{2/3}[\text{Mn}_{0.7}\text{Zn}_{0.3}]\text{O}_2$, for which the combination of $\text{O}^{2-/1-}$ and $\text{Mn}^{4+/3+}$ contributed to rechargeable capacity.^[23] Kim et al.^[24] observed the oxygen redox in P2- $\text{Na}_{2/3}[\text{Mg}_{0.2}\text{Mn}_{0.6}\text{Co}_{0.2}]\text{O}_2$, which enabled long-term cycling assisted by the presence of Co–O bonds, facilitating electron transfer with the overlapping of orbitals between $\text{O}^{2-} 2p$ and $\text{Co}^{3+/4+} 3d (t_{2g})$. Despite these successes of the oxygen redox reaction toward contributing additional capacity in P2-layered compounds, the main shortcoming is that the resulting operation voltage remains still low because the main redox species of $\text{Mn}^{4+/3+}$ is achieved in the voltage range of 1.5–2.7 V versus Na^+/Na .

This issue motivated us to raise the operation voltage, such that a solid solution of $\text{Na}_{2/3}[\text{Ni}^{2+}_{0.3}\text{Mn}^{4+}_{0.7}]\text{O}_2$ and $\text{Na}_{2/3}[\text{Zn}^{2+}_{0.3}\text{Mn}^{4+}_{0.7}]\text{O}_2$, of which the latter is activated by only an oxygen redox process during the first charge, is proposed as $\text{Na}_{2/3}[(\text{Ni}_{0.5}\text{Zn}_{0.5})_{0.3}\text{Mn}_{0.7}]\text{O}_2$. As anticipated, the average operating voltage increased from 2.6 to 3.5 V for $\text{Na}_{2/3}[(\text{Ni}_{0.5}\text{Zn}_{0.5})_{0.3}\text{Mn}_{0.7}]\text{O}_2$ (105 mAh g^{-1}) on discharge in the voltage range of 2.3–4.6 V. Operando X-ray diffraction studies demonstrated that the P2 phase was transformed to the OP4 phase on charge and then returned to the original P2 phase. Ex situ X-ray photoelectron spectroscopy (XPS) and X-ray absorption near edge structure (XANES) spectroscopy results indicated that the electrochemical activities are related to the two-electron reaction of $\text{Ni}^{2+/4+}$ and additional $\text{O}^{2-/1-}$ redox pairs. The $\text{Na}_{2/3}[(\text{Ni}_{0.5}\text{Zn}_{0.5})_{0.3}\text{Mn}_{0.7}]\text{O}_2$ electrode was able to retain its initial capacity (105 mAh g^{-1}) over 95% during 200 cycles not only at 26 mA g^{-1} (0.1C) but also at a high rate (2.6 A g^{-1} , 10C) with a capacity of 76 mAh g^{-1} . The combination of two redox species, the $\text{Ni}^{2+/4+}$ pair responsible for raising the operation voltage and the $\text{O}^{2-/1-}$ couple appearing over 4.2 V resulting in additional capacity, is responsible for the increase in energy density, while the inactive tetravalent Mn helps maintain the structure for prolonged cycling. Furthermore, it was confirmed through first-principles calculation that Na^+ de/intercalation at the $\text{Na}_{2/3}[(\text{Ni}_{0.5}\text{Zn}_{0.5})_{0.3}\text{Mn}_{0.7}]\text{O}_2$ electrode was determined by the oxidation/reduction of not only Mn and Ni ions but also O ions.

2. Results and Discussion

The crystal structure of the as-synthesized P2- $\text{Na}_{2/3}[(\text{Ni}_{0.5}\text{Zn}_{0.5})_{0.3}\text{Mn}_{0.7}]\text{O}_2$, for which the chemical composition was analyzed by inductively coupled plasma-atomic emission spectroscopy (Table S1, Supporting Information), was refined assuming $P6_3/mmc$ space group. This

result indicates that the synthesized material was crystallized into a single phase (Figure 1a). The lattice parameters obtained from the Rietveld refinement showed a slight decrease in the lattice parameters after incorporation of Ni into $\text{Na}_{2/3}[\text{Zn}_{0.3}\text{Mn}_{0.7}]\text{O}_2$; specifically, $a = 2.8939(3) \text{ \AA}$ and $c = 11.1465(7) \text{ \AA}$ for $\text{Na}_{2/3}[(\text{Ni}_{0.5}\text{Zn}_{0.5})_{0.3}\text{Mn}_{0.7}]\text{O}_2$, whereas $a = 2.9004(3) \text{ \AA}$ and $c = 11.1842(6) \text{ \AA}$ for $\text{Na}_{2/3}[\text{Zn}_{0.3}\text{Mn}_{0.7}]\text{O}_2$ (Table S2, Supporting Information). The average oxidation states of Ni and Mn investigated by XANES spectroscopy present that Ni and Mn were stabilized as Ni^{2+} and Mn^{4+} for $\text{Na}_{2/3}[(\text{Ni}_{0.5}\text{Zn}_{0.5})_{0.3}\text{Mn}_{0.7}]\text{O}_2$ (Figure 1b). This variation likely originated from the slight difference in the ionic radii between Ni^{2+} (0.69 Å) and Zn^{2+} (0.74 Å). TEM analysis revealed that the micron-sized particle was homogeneously composed of Na, Ni, Zn, and Mn elements (Figure 1c).

The electrochemical properties of P2- $\text{Na}_{2/3}[(\text{Ni}_{0.5}\text{Zn}_{0.5})_{0.3}\text{Mn}_{0.7}]\text{O}_2$ was investigated in the voltage range of 2.3–4.6 V (Figure 2). The P2- $\text{Na}_{2/3}[(\text{Ni}_{0.5}\text{Zn}_{0.5})_{0.3}\text{Mn}_{0.7}]\text{O}_2$ delivered a first charge capacity of $\approx 130 \text{ mAh g}^{-1}$ at a current of 26 mA g^{-1} (0.1C), with a two-step process; namely, a slope from 3.2–4.1 V and a flat plateau above 4.1 V (Figure 2a). This tendency differs from the charging behavior of P2- $\text{Na}_{2/3}[\text{Zn}_{0.3}\text{Mn}_{0.7}]\text{O}_2$, which consists of a flat voltage profile over 4.1 V because of the only electrochemical oxidation of oxygen from the oxide lattice, as reported in our prior work.^[23] It is assumed that the oxidation of $\text{Ni}^{2+/4+}$ is related to the slope between 3.2 and 4.1 V for the present $\text{Na}_{2/3}[(\text{Ni}_{0.5}\text{Zn}_{0.5})_{0.3}\text{Mn}_{0.7}]\text{O}_2$. Although the length of the plateau decreased, the delivered charge capacity for $\text{Na}_{2/3}[(\text{Ni}_{0.5}\text{Zn}_{0.5})_{0.3}\text{Mn}_{0.7}]\text{O}_2$ was higher than that for $\text{Na}_{2/3}[\text{Zn}_{0.3}\text{Mn}_{0.7}]\text{O}_2$ (115 mAh g^{-1}).^[23] The electrode delivered capacity of 105 mAh g^{-1} on discharge. Usually, P2-type electrodes suffers from the abnormal low Coulombic efficiency (CE) at the initial cycle, however, the P2- $\text{Na}_{2/3}[\text{Zn}_{0.3}\text{Mn}_{0.7}]\text{O}_2$ electrode exhibited high CE, which benefits in full cell configuration. From the discharge profile, it is thought that the $\text{Mn}^{4+/3+}$ redox may not be available in this operation condition, such that the effect of Jahn–Teller distortion over Mn^{3+}O_6 octahedra, which emerges when deeply sodiated to 1.5 V, can be excluded for the present work. The dQ/dV plots indicated that an emerged large peak at 4.2 V at the first charge weakened while reversible after the first cycle (Figure S1, Supporting Information). As observed in Figure 2b, the capacity retention was markedly improved to 95% with an energy density $>300 \text{ Wh kg}^{-1}$ over 200 cycles. The ac-impedance studies presented that the slight increase in the impedance would be associated with decomposition of electrolyte during high voltage operation (Figure S2, Supporting Information). In addition, the P2- $\text{Na}_{2/3}[(\text{Ni}_{0.5}\text{Zn}_{0.5})_{0.3}\text{Mn}_{0.7}]\text{O}_2$ exhibited excellent rate capability, even at a high current density of 2.6 A g^{-1} (10C), delivering approximately 70% of its capacity obtained at 0.1C (Figure 2c,d).

Operando XRD (*o*-XRD) analysis was performed to understand the structural change of the P2- $\text{Na}_{2/3}[(\text{Ni}_{0.5}\text{Zn}_{0.5})_{0.3}\text{Mn}_{0.7}]\text{O}_2$ during de-/sodiation (Figure 3a and Figure S3, Supporting Information). During the first charge process, the (002) and (004) peaks of the P2 phase shifted toward lower angle (2θ), whereas the (100) and (102) peaks of the P2 phase shifted to higher angle (2θ). This tendency is associated with sodium ions being removed from the crystal structure, leading to interlayer expansion as the increased repulsive force in the oxide lattice resulted in an increase in the *c*-axis parameter (Figure 3b). In addition,

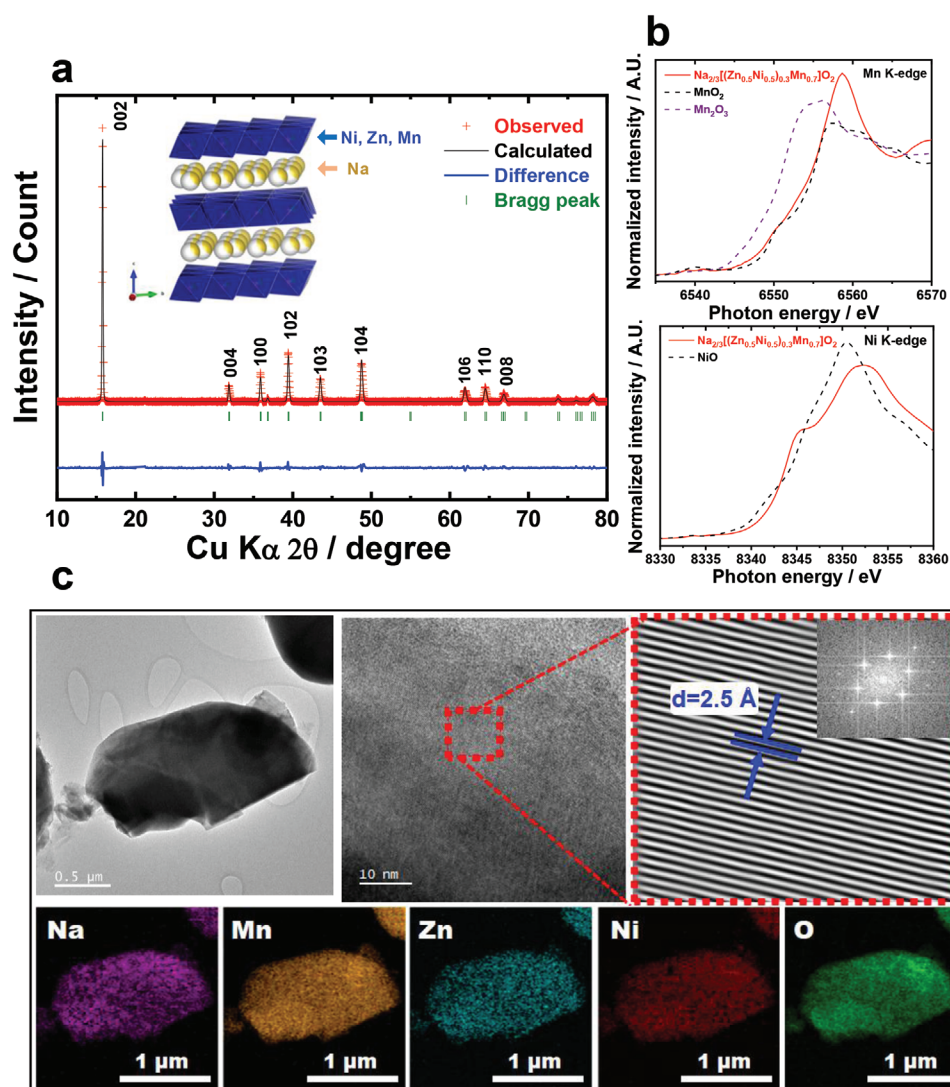


Figure 1. a) Rietveld refinement of crystal structure, b) XANES spectra, c) TEM and EDS mapping results for $\text{P2-Na}_{2/3}[(\text{Ni}_{0.5}\text{Zn}_{0.5})_{0.3}\text{Mn}_{0.7}]\text{O}_2$.

it is possible that the oxidation of transition metals reduced the Ni–O distance, as Mn^{4+} is inactive on oxidation, resulting in a decrease of the a -axis parameter during desodiation. Increasing the operation voltage to 4 V induced broadening of the XRD peaks, and the peak shifted toward a higher angle from 4 V, which is related to the occurrence of a phase transition (Figure 3a). The (002) peak of the OP4 phase appeared at 17.5° (2θ) at the end of the charge. In this regime of the OP4 phase, it is interesting to see that the a -axis parameter was continuously lowered (Figure 3b). According to the literature,^[25] $\text{P2-Na}_{2/3}[\text{Ni}_{1/3}\text{Mn}_{2/3}]\text{O}_2$ undergoes a phase transition to an O2 phase, with a (002) peak at $\approx 18.5^\circ$ (2θ), because of desodiation, accompanied by a drastic volume change of $\approx 23\%$. The difference in the peak position is interpreted as transformation of the phase to OP4 with reduced volume change. The reversible behavior was evident on discharge, with the (002) peak of the OP4 phase recovered to the original P2 phase. During the second charge, the same tendency as that during the first charge was observed, indicating the reversibility of the phase

transition between P2 and OP4. The small change in volume ($\Delta V \approx 5\%$) during charge and discharge and suppression of the transition to the O2 phase positively affected the cycling performance of the electrode, as $\text{P2-Na}_{2/3}[(\text{Ni}_{0.5}\text{Zn}_{0.5})_{0.3}\text{Mn}_{0.7}]\text{O}_2$ displayed excellent cyclability (Figure 2).

We further correlated the oxidation states of the transition metals and oxygen to the structural change observed in the o -XRD analysis (Figure 3). **Figure 4a** presents ex situ XANES data for the Mn K-edge, which indicates that the oxidation state of manganese is close to 4^+ for the fresh state. Upon charging to 4.6 V, there was no change in the oxidation state of Mn, as oxidation beyond 4^+ is not possible in the operation window of 2.3–4.6 V. Discharging to 2.3 V did not alter the oxidation state of Mn, as the $\text{Mn}^{4+/3+}$ redox is inactive in this voltage range. This finding validates that the tetravalent Mn provides structural stability for $\text{P2-Na}_{2/3}[(\text{Ni}_{0.5}\text{Zn}_{0.5})_{0.3}\text{Mn}_{0.7}]\text{O}_2$ when it cycled in the range of 2.3–4.6 V. The Ni K-edge spectra show that the divalent Ni is oxidized to tetravalent Ni on charge (Figure 4b). Considering that the theoretical capacity from the oxidation of

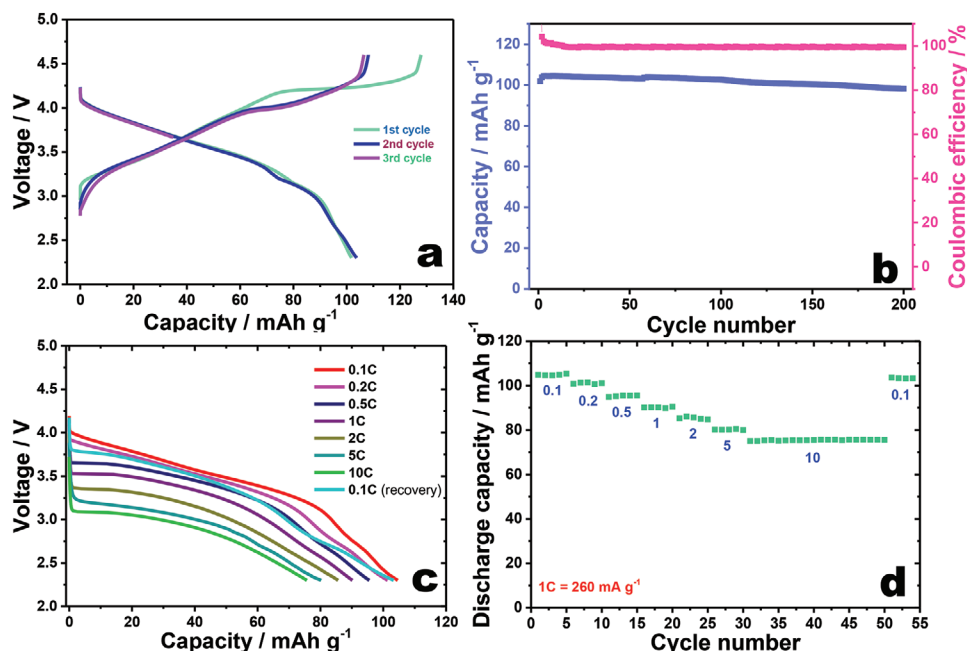


Figure 2. a) Voltage profiles of initial cycles, b) cycling performance at current density of 26 mA g^{-1} in the voltage range of 2.3–4.6 V, and c,d) rate capability of $\text{P2-Na}_{2/3}[(\text{Ni}_{0.5}\text{Zn}_{0.5})_{0.3}\text{Mn}_{0.7}]\text{O}_2$ at different current densities.

0.15 mole of divalent Ni to tetravalent Ni is $\approx 80 \text{ mAh g}^{-1}$, it is reasonable that the 74 mAh g^{-1} of capacity delivered to 4.1 V is assisted by the oxidation of Ni^{2+} to Ni^{4+} on charge. During discharging to 2.3 V, the oxidized Ni^{4+} is reduced to Ni^{2+} . As shown in Figure 2a, the capacity delivered during the charging process is $\approx 130 \text{ mAh g}^{-1}$; thus, the $\text{Ni}^{2+/4+}$ pair resulted in $\approx 74 \text{ mAh g}^{-1}$ of capacity, while oxidation Mn^{4+} was not involved in the electrochemical reaction in this voltage range (Figure 4a). Hence, it is hypothesized that the extra capacity of $\approx 56 \text{ mAh g}^{-1}$ may result from the oxidation of oxygen from the oxide lattice. To confirm this assumption, the O K-edge spectrum of the fresh state for $\text{P2-Na}_{2/3}[(\text{Ni}_{0.5}\text{Zn}_{0.5})_{0.3}\text{Mn}_{0.7}]\text{O}_2$ was compared with that charged to 4.6 V and discharged 2.3 V (Figure 3c). Charging to 4.6 V varied the intensity of the pre-edge (535 eV), indicating a change in the charge state of oxygen from O^{2-} to O^{1-} . As observed in Figure 3c, it is interesting that the calculated a -axis

parameter gradually decreased even above 4.2 V, even though Mn was inactive at the first charge. Hence, it is thought that the progressive oxidation of oxygen in the oxide lattice is responsible for the continuous decrease in the a -axis parameter. In addition, the O K-edge spectrum was recovered to the original state after discharging to 2.3 V because of the reduction of oxygen from O^{1-} to O^{2-} . This reaction contributes to the extra capacity of approximately 56 mAh g^{-1} on charge over 4.1 V and 45 mAh g^{-1} in the range of 3.5–4.6 V on discharge. The stable cyclability shown in Figure 2b, with over 95% capacity retention for 200 cycles, indicates that the oxidation and reduction of oxygen are quite reversible during the cycling.

Ex situ XPS analysis of O1s further supports the validity of the oxygen redox observed in $\text{P2-Na}_{2/3}[(\text{Ni}_{0.5}\text{Zn}_{0.5})_{0.3}\text{Mn}_{0.7}]\text{O}_2$ (Figure S4, Supporting Information). Because surface deposits can lead to misinterpretation of the data, the surface was etched with Ar^+ for 10 min in macro mode ($3 \times 3 \text{ mm}^2$), corresponding to 22 nm in depth using a standard Si reference, where the depth is regarded as the bulk of the $\text{P2-Na}_{2/3}[(\text{Ni}_{0.5}\text{Zn}_{0.5})_{0.3}\text{Mn}_{0.7}]\text{O}_2$. The obtained data revealed two main peaks in the oxygen spectrum of the pristine electrode. The peak at 530 eV is related to the Me–O bond, where oxygen bonds with the transition metal, and the peak at $\approx 532 \text{ eV}$ is associated with the oxygen of the surface deposits such as Na_2CO_3 .^[26,27] After charging to 4.6 V, a new peak appeared at 531 eV, and the intensity arose from the decrease of the Me–O peak. The appearance of this new peak is attributed to the oxidation of oxygen of the oxide lattice during the extraction of sodium ions from the crystal structure. After discharge, the new peak disappeared and the relative intensity of the Me–O binding energy increased again. This tendency indicates that the change in the chemical state of oxygen is reversible,

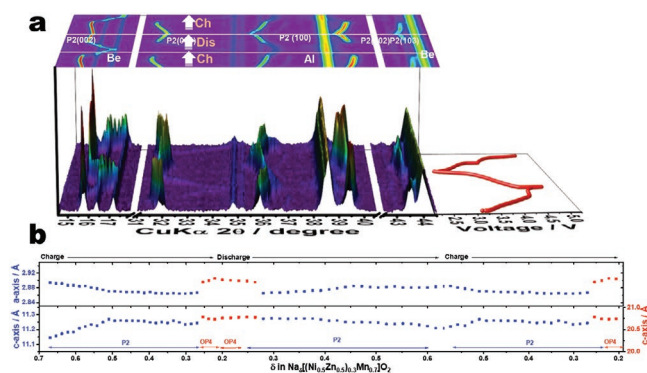


Figure 3. Operando XRD patterns of $\text{P2-Na}_{2/3}[(\text{Ni}_{0.5}\text{Zn}_{0.5})_{0.3}\text{Mn}_{0.7}]\text{O}_2$ in a) 3D and b) change of lattice parameters during cycling.

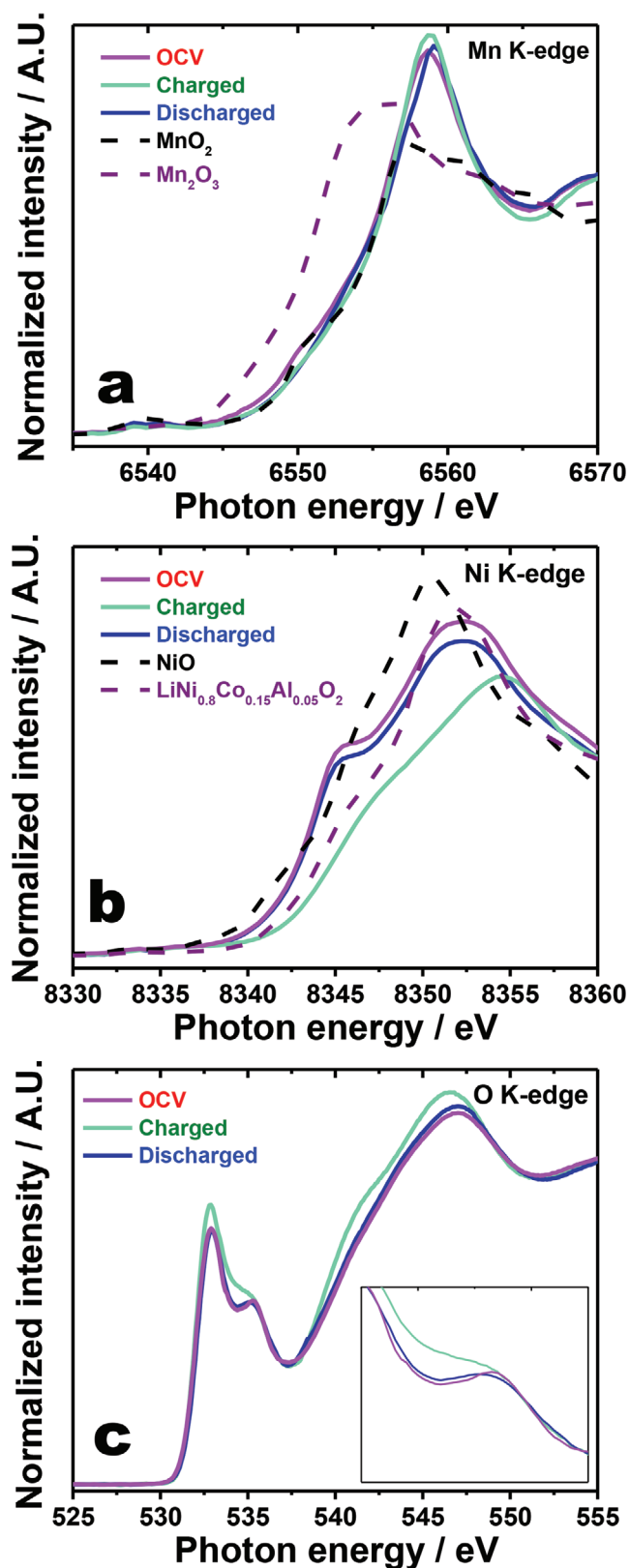


Figure 4. Ex situ XANES spectra before and after the first charge and discharge: a) Mn K edge, b) Ni K edge, and c) O K edge for $\text{P2-Na}_{2/3}[(\text{Ni}_{0.5}\text{Zn}_{0.5})_{0.3}\text{Mn}_{0.7}]\text{O}_2$.

which is consistent with the XANES analysis for the O K-edge (Figure 4c). Therefore, the oxygen redox couple contributes to the delivery of extra capacity over 4.1 V, as evidenced by the *o*-XRD, XANES, and XPS results.

In addition, based on the structural information of $\text{Na}_{2/3}[(\text{Ni}_{0.5}\text{Zn}_{0.5})_{0.3}\text{Mn}_{0.7}]\text{O}_2$, we performed first-principles calculation for prediction of theoretical reaction mechanism on the Na^+ de/intercalation of $\text{Na}_{2/3}[(\text{Ni}_{0.5}\text{Zn}_{0.5})_{0.3}\text{Mn}_{0.7}]\text{O}_2$. In particular, because it was verified that $\text{Na}_{2/3}[(\text{Ni}_{0.5}\text{Zn}_{0.5})_{0.3}\text{Mn}_{0.7}]\text{O}_2$ experiences oxygen-redox reaction during charging, it is required to correct the self-interaction errors on not only metal ions but also oxygen ions for first-principles calculation. Thus, we applied density functional theory (DFT) with the Heyd–Scuseria–Ernzerhof (HSE06) hybrid functional to predict the theoretical reaction mechanism of $\text{Na}_{2/3}[(\text{Ni}_{0.5}\text{Zn}_{0.5})_{0.3}\text{Mn}_{0.7}]\text{O}_2$.^[10,28] Figure 5 shows the projected density of states (pDOS) of various $\text{Na}_x[(\text{Ni}_{0.125}\text{Zn}_{0.125}\text{Mn}_{0.75}]\text{O}_2$ ($\approx \text{Na}_x[(\text{Ni}_{0.5}\text{Zn}_{0.5})_{0.3}\text{Mn}_{0.7}]\text{O}_2$). During Na^+ deintercalation from $\text{Na}_1[(\text{Ni}_{0.125}\text{Zn}_{0.125}\text{Mn}_{0.75}]\text{O}_2$ to $\text{Na}_{0.5}[(\text{Ni}_{0.125}\text{Zn}_{0.125}\text{Mn}_{0.75}]\text{O}_2$, the electron densities of Mn 3d orbitals neighboring Fermi level (E_F) decreased more than those of Ni 3d and O 2p orbitals neighboring E_F , which indicates $\text{Mn}^{3+}/\text{Mn}^{4+}$ redox reaction between $\text{Na}_1[(\text{Ni}_{0.125}\text{Zn}_{0.125}\text{Mn}_{0.75}]\text{O}_2$ and $\text{Na}_{0.5}[(\text{Ni}_{0.125}\text{Zn}_{0.125}\text{Mn}_{0.75}]\text{O}_2$ (Figure 5a). And then, it was predicted that the intensity of electron densities on Ni 3d orbitals near E_F is highly decreased to approximately zero after 0.25 mol Na^+ deintercalation at $\text{Na}_{0.5}[(\text{Ni}_{0.125}\text{Zn}_{0.125}\text{Mn}_{0.75}]\text{O}_2$ (Figure 5b). It implies that the electrons in Ni ions are mainly used for Na^+ deintercalation between $\text{Na}_{0.5}[(\text{Ni}_{0.125}\text{Zn}_{0.125}\text{Mn}_{0.75}]\text{O}_2$ and $\text{Na}_{0.25}[(\text{Ni}_{0.125}\text{Zn}_{0.125}\text{Mn}_{0.75}]\text{O}_2$. In case of $\text{Na}_{0.25}[(\text{Ni}_{0.125}\text{Zn}_{0.125}\text{Mn}_{0.75}]\text{O}_2$, the electron densities near E_F are mostly composed of O 2p orbitals (Figure 5c top). After full Na deintercalation from $\text{Na}_{0.25}[(\text{Ni}_{0.125}\text{Zn}_{0.125}\text{Mn}_{0.75}]\text{O}_2$ to $\text{Na}_0[(\text{Ni}_{0.125}\text{Zn}_{0.125}\text{Mn}_{0.75}]\text{O}_2$, many hole densities of O 2p orbitals are generated (Figure 5d top). These predictions implies occurrence of the $\text{O}^{2-/1-}$ redox reaction of $\text{Na}_x[(\text{Ni}_{0.125}\text{Zn}_{0.125}\text{Mn}_{0.75}]\text{O}_2$, which is well consistent with research results of the previous papers reporting the $\text{O}^{2-/1-}$ redox reaction of electrode materials for LIBs and SIBs.^[10,23] In addition, to verify the change from electron densities to hole densities at the O 2p orbital $\text{Na}_x[(\text{Ni}_{0.125}\text{Zn}_{0.125}\text{Mn}_{0.75}]\text{O}_2$ during Na^+ deintercalation in detail, we visualized the charge densities on the O 2p orbital. In case of $\text{Na}_{0.25}[(\text{Ni}_{0.125}\text{Zn}_{0.125}\text{Mn}_{0.75}]\text{O}_2$, electron densities are observed in the O 2p orbital of each Na–O–Zn bonding at the range between -0.5 and -1.5 eV (Figure 5c bottom). After Na^+ deintercalation from $\text{Na}_{0.25}[(\text{Ni}_{0.125}\text{Zn}_{0.125}\text{Mn}_{0.75}]\text{O}_2$ to $\text{Na}_0[(\text{Ni}_{0.125}\text{Zn}_{0.125}\text{Mn}_{0.75}]\text{O}_2$, the electron densities in the O 2p orbital of each Na–O–Zn bonding are transformed to hole densities (Figure 5d bottom). These results indicates that Na^+ ions in $\text{Na}_x[(\text{Ni}_{0.125}\text{Zn}_{0.125}\text{Mn}_{0.75}]\text{O}_2$ are de/intercalated by $\text{O}^{2-/1-}$ redox reaction.

Moreover, the overall reaction mechanism of $\text{Na}_x[(\text{Ni}_{0.125}\text{Zn}_{0.125}\text{Mn}_{0.75}]\text{O}_2$ are also confirmed through the comparison of the integrated spin moments on Ni and O ions among various $\text{Na}_x[(\text{Ni}_{0.125}\text{Zn}_{0.125}\text{Mn}_{0.75}]\text{O}_2$ compositions. As presented in Figure 6a,b, the net magnetic moments of Ni and O ions are approximately changed from +2 to 0, and from 0 to +1, respectively, which means that $\text{Ni}^{2+/4+}$ and $\text{O}^{2-/1-}$ redox reactions occur during Na^+ de/intercalation. This prediction based on first-principles calculation are consistent with the experimental results identified through the ex situ XANES and XPS

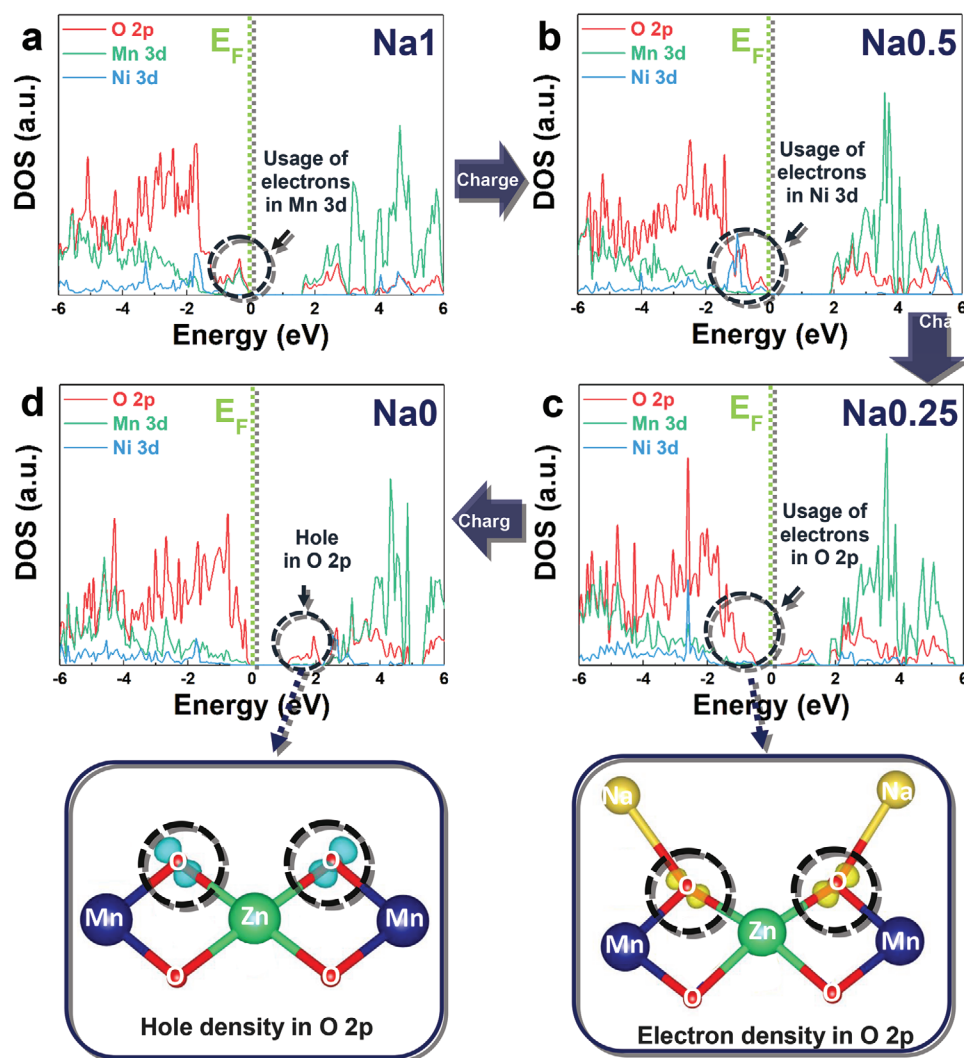


Figure 5. pDOS of O 2p, Mn 3d and Ni 3d orbitals on a) $\text{Na}_1[\text{Ni}_{0.125}\text{Zn}_{0.125}\text{Mn}_{0.75}]\text{O}_2$, b) $\text{Na}_{0.5}[\text{Ni}_{0.125}\text{Zn}_{0.125}\text{Mn}_{0.75}]\text{O}_2$, c) $\text{Na}_{0.25}[\text{Ni}_{0.125}\text{Zn}_{0.125}\text{Mn}_{0.75}]\text{O}_2$ and d) $\text{Na}_0[\text{Ni}_{0.125}\text{Zn}_{0.125}\text{Mn}_{0.75}]\text{O}_2$.

analyses mentioned above. The possible reaction mechanism is described in Figure 6c.

We compared the capacity and average operation voltages of $\text{P2-Na}_{2/3}[(\text{Ni}_{0.5}\text{Zn}_{0.5})_{0.3}\text{Mn}_{0.7}]\text{O}_2$ to those of other compounds assisted by oxygen redox (Figure 7 and Table S3, Supporting Information). It is clear that the average operation voltages differ from those of the main transition metal species. Among cathode materials, the present $\text{P2-Na}_{2/3}[(\text{Ni}_{0.5}\text{Zn}_{0.5})_{0.3}\text{Mn}_{0.7}]\text{O}_2$ exhibits not only a reasonably high operation of 3.5 V but also excellent capacity retention. The excellent performance was achieved due to the crystal structure being stable as shown in Figure S5 (Supporting Information). The XRD of cycled electrode shows that the crystal structure remains almost the same as the fresh electrode with slight lattice change (Table S4, Supporting Information). As designed, it is important to select the main transition metal redox center to increase the operating voltage, which is directly related to energy density, for which the redox potential of $\text{Ni}^{2+}/\text{Ni}^{4+}$ and $\text{O}^{2-}/\text{O}^{1-}$ appears to be promising for long term cycles.

3. Conclusion

In summary, the operating voltage of the P2-type $\text{Na}_{2/3}[\text{Zn}_{0.3}\text{Mn}_{0.7}]\text{O}_2$ electrode was increased by introducing the electrochemical active Ni on the Zn site. The resulting P2-type $\text{Na}_{2/3}[(\text{Ni}_{0.5}\text{Zn}_{0.5})_{0.3}\text{Mn}_{0.7}]\text{O}_2$ electrode displayed excellent electrochemical performance, the operating voltage was raised from 2.6 to 3.5 V with retention of 95% of its initial capacity after 200 cycles. Operando XRD analysis revealed that a P2-OP4 phase transition occurs during charge and discharge. Ex situ XANES and XPS analyses proved that the capacity above 4.1 V is contributed by the oxygen redox, and the capacity below 4.1 V is delivered by the $\text{Ni}^{2+}/\text{Ni}^{4+}$ redox. Furthermore, we confirmed using first-principles calculation that $\text{Na}_x[(\text{Ni}_{0.5}\text{Zn}_{0.5})_{0.3}\text{Mn}_{0.7}]\text{O}_2$ experiences not only cationic $\text{Ni}^{2+}/\text{Ni}^{4+}$ redox reactions but also anionic redox reaction of $\text{O}^{2-}/\text{O}^{1-}$. As a result, we designed a high-voltage Mn-rich cathode material for SIBs, and we believe our finding will open up a pathway for further development of high-voltage anionic-based materials.

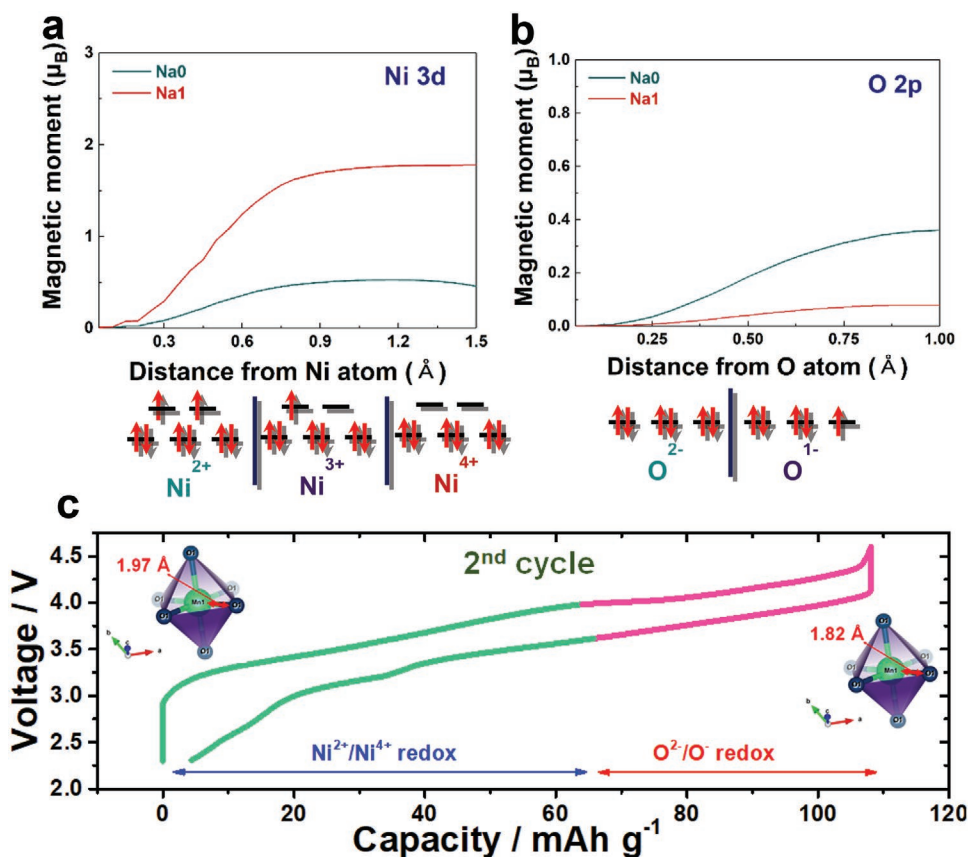


Figure 6. Comparison of integrated spin moments on a) Ni 3d and b) O 2p orbitals between $\text{Na}_1[\text{Ni}_{0.125}\text{Zn}_{0.125}\text{Mn}_{0.75}]\text{O}_2$ and $\text{Na}_0[\text{Ni}_{0.125}\text{Zn}_{0.125}\text{Mn}_{0.75}]\text{O}_2$. c) Schematic illustration of the reaction mechanism of the P2- $\text{Na}_{2/3}[(\text{Ni}_{0.5}\text{Zn}_{0.5})_{0.3}\text{Mn}_{0.7}]\text{O}_2$ electrode.

4. Experimental Section

Synthesis: The conventional self-combustion method, as described in our prior work,^[29] was used to synthesize the desired P2 layered compounds. Starting nitrate salts such as sodium, manganese, zinc, and nickel were dissolved in distilled water, followed by the addition of citric acid as a fuel (nitrates: citric acid, 1:0.2 by weight). Once the salts were completely dissolved, the solution was heated at 100 °C to evaporate the aqueous solution. Afterward, the obtained powders were heated at 200 °C to initiate self-combustion. Then, the burnt powders were again heat-treated at 500 °C for 3 h in air to enable decomposition of the used nitrates and carbon

residues in the product. The obtained powders were pelletized and heated in a tube furnace at 900 °C for 10 h in an air atmosphere and then allowed to slowly cool to room temperature. The obtained powder was transferred to an Ar-filled glove box to avoid contact with moisture in the air.

Characterization: X-ray diffraction (XRD, X'Pert, PANalytical) using Cu-K α radiation was employed to characterize the crystal structure of the synthesized powders, and the obtained XRD data were analyzed by the FULLPROF Rietveld program.^[30] The obtained products were examined using high-resolution transmission electron microscopy (HRTEM; JEM-ARM200F, JEOL). The structural evolution of the cathode materials was monitored using operando XRD (o-XRD) during de-/sodiation. The oxidation state changes for the transition metals and oxygen were analyzed by ex situ XANES spectroscopy and XPS. Ex situ XANES measurements were performed at beamline 4D for oxygen and beamline 8C for transition metals at the Pohang Accelerator Laboratory (PAL), Pohang, South Korea. The analysis of Mn K-edge was done in five energy steps with different integration time; first energy step and integration time: 5 eV and 1 s, second energy step and integration time: 2.5 eV and 1 s, third energy step and integration time: 0.2 eV and 1 s, fourth energy step and integration time: 0.03 keV and 1 s, and fifth energy step and integration time: 0.04 keV and 1 s from 6339.002 eV (E_0). The spectra for the O K-edge were measured using a synchrotron radiation photoemission spectroscopy with the incident X-ray source at 650 eV and have three energy steps with different integration time; first energy step and integration time: 0.3 eV and 1 s, second energy step and integration time: 0.2 eV and 1 s, and third energy step and integration time: 0.4 keV and 1 s from 525.000 eV (E_0). The obtained data were analyzed using the Athena software.^[31]

Electrochemical Test: The prepared active materials were blended with Super-P and polyvinylidene fluoride (PVDF) in a weight ratio of 8:1:1 in N-methyl-2-pyrrolidone (NMP). The obtained slurry was placed on Al foil and dried at 80 °C overnight under vacuum. Electrochemical cell tests of

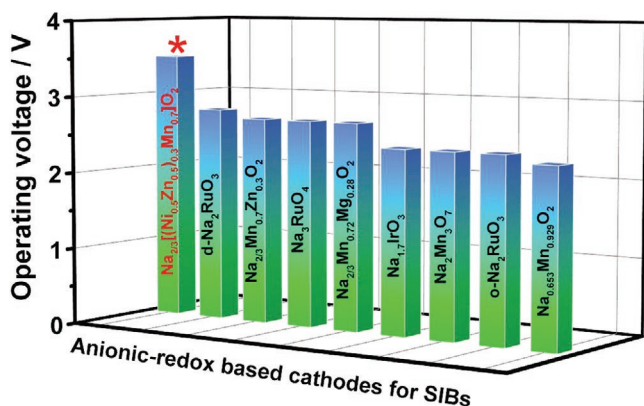


Figure 7. Comparison of average operating voltage of oxygen-redox based sodium cathode materials.

a cathode (typical active material loading of 3.0 mg cm^{-2}) were conducted after assembling an R2032 coin-type cell using sodium metal as the negative electrode in an Ar-filled glove box. The electrolyte solution consisted of 0.5 M NaPF_6 in propylene carbonate (PC) and fluorinated ethylene carbonate (FEC) (98:2 in volume). The cells were charged and discharged between 2.3 and 4.6 V at a rate of 0.1C ($1\text{C} = 260 \text{ mA g}^{-1}$) at 25°C .

Surface Analysis: After the polarization in transient mode, the scratched surface of each type 316L stainless steel specimen was investigated using ToF-SIMS (PHI TRIFT V nanoTOF). The total collection time was 240 s over a $12 \times 12 \mu\text{m}^2$ area on the scratched surface etched by Ga^+ ions over a $400 \times 400 \mu\text{m}^2$ area for 100 s. The surface of each specimen was also examined using XPS (ULVAC-PHI 5600) to evaluate the thickness and chemical states of the passive layers formed during polarization. For the depth profile, the Ar^+ etching sputter rate was determined to be 2.2 nm min^{-1} over a $400 \times 400 \mu\text{m}^2$ area on the surface of each specimen.

Computational Details: The Vienna ab initio simulation package (VASP) for density functional theory (DFT) based first-principles calculations was used.^[32–34] For accurate prediction, the pseudopotentials of projector augmented-wave (PAW)^[35] with a plane-wave basis set and the Heyd–Scuseria–Ernzerhof (HSE06) hybrid functional were applied.^[28] All DFT calculations were performed with the energy cutoff of 500 eV. The crystal structure of P2-type $\text{Na}_x[\text{Ni}_{0.125}\text{Zn}_{0.125}\text{Mn}_{0.75}]\text{O}_2$ ($x = 0, 0.25, 0.5$ and 1) with a $2 \times 2 \times 1$ supercell was used. Numerous Ni/Zn/Mn ordering and Na/vacancy ordering were prepared using CASM software,^[36] and then, the most stable P2-type $\text{Na}_x[\text{Ni}_{0.125}\text{Zn}_{0.125}\text{Mn}_{0.75}]\text{O}_2$ structures through comparison of the electrostatic energies and DFT energies was determined. The DFT energies were evaluated within the generalized gradient approximation (GGA)+U.^[37] The U values of 6.0 and 3.9 eV were used for Ni and Mn, respectively.^[10] To optimize the structural information such as lattice parameters and atomic positions, the residual forces that are smaller than 0.03 eV \AA^{-1} are required.

Supporting Information

Supporting Information is available from the Wiley Online Library or from the author.

Acknowledgements

This research was supported by the Basic Science Research Program through the National Research Foundation of Korea (NRF), funded by the Ministry of Education, Science, and Technology of Korea (NRF-2017R1A2A2A05069634 and NRF-2015M3D1A1069713), Ministry of Science and ICT of Korea (NRF-2019H1D8A2106002).

Conflict of Interest

The authors declare no conflict of interest.

Keywords

oxygen redox, P2-type cathodes, sodium-ion batteries

Received: March 29, 2020

Revised: April 20, 2020

Published online: May 7, 2020

[1] G. Assat, J. M. Tarascon, *Nat. Energy* **2018**, *3*, 373.

[2] G. Assat, D. Foix, C. Delacourt, A. Iadecola, R. Dedryvère, J. M. Tarascon, *Nat. Commun.* **2017**, *8*, 2219.

- [3] N. Yabuuchi, *Chem. Lett.* **2017**, *46*, 412.
- [4] N. Yabuuchi, K. Kubota, M. Dahbi, S. Komaba, *Chem. Rev.* **2014**, *114*, 11636.
- [5] J. Y. Hwang, S. T. Myung, Y. K. Sun, *Chem. Soc. Rev.* **2017**, *46*, 3529.
- [6] C. Delmas, *Adv. Energy Mater.* **2018**, *8*, 1703137.
- [7] M. H. Han, E. Gonzalo, G. Singh, T. Rojo, *Energy Environ. Sci.* **2015**, *8*, 81.
- [8] N. Ortiz-Vitoriano, N. E. Drewett, E. Gonzalo, T. Rojo, *Energy Environ. Sci.* **2017**, *10*, 1051.
- [9] M. Sathiya, G. Rousse, K. Ramesha, C. P. Laisa, H. Vezin, M. T. Sougrati, M. L. Doublet, D. Foix, D. Gonbeau, W. Walker, A. S. Prakash, M. Ben Hassine, L. Dupont, J. M. Tarascon, *Nat. Mater.* **2013**, *12*, 827.
- [10] D. H. Seo, J. Lee, A. Urban, R. Malik, S. Kang, G. Ceder, *Nat. Chem.* **2016**, *8*, 692.
- [11] Z. Lu, J. R. Dahn, *J. Electrochem. Soc.* **2002**, *149*, A815.
- [12] A. D. Robertson, P. G. Bruce, *Chem. Mater.* **2003**, *15*, 1984.
- [13] H. Koga, L. Croguennec, M. Ménétrier, P. Mannesiez, F. Weill, C. Delmas, S. Belin, *J. Phys. Chem. C* **2014**, *118*, 5700.
- [14] X. Cao, X. Li, Y. Qiao, M. Jia, F. Qiu, Y. He, P. He, H. Zhou, *ACS Energy Lett.* **2019**, *4*, 2409.
- [15] Z. N. Taylor, A. J. Perez, J. J. Coca-Clemente, F. Braga, N. E. Drewett, M. J. Pitcher, W. J. Thomas, M. S. Dyer, C. Collins, M. Zanella, T. Johnson, S. Day, C. Tang, V. R. Dhanak, J. B. Claridge, L. J. Hardwick, M. J. Rosseinsky, *J. Am. Chem. Soc.* **2019**, *141*, 7333.
- [16] W. Yang, T. P. Devereaux, *J. Power Sources* **2018**, *389*, 188.
- [17] Y. Qiao, S. Guo, K. Zhu, P. Liu, X. Li, K. Jiang, C. J. Sun, M. Chen, H. Zhou, *Energy Environ. Sci.* **2018**, *11*, 299.
- [18] P. E. Pearce, G. Rousse, O. M. Karakulina, J. Hadermann, G. Van Tendeloo, D. Foix, O. Fauth, A. M. Abakumov, J.-M. Tarascon, *Chem. Mater.* **2018**, *30*, 3293.
- [19] B. Mortemard De Boisse, G. Liu, J. Ma, S. I. Nishimura, S. C. Chung, H. Kiuchi, Y. Harada, J. Kikkawa, Y. Kobayashi, M. Okubo, A. Yamada, *Nat. Commun.* **2016**, *7*, 11397.
- [20] N. Yabuuchi, R. Hara, M. Kajiyama, K. Kubota, T. Ishigaki, A. Hoshikawa, S. Komaba, *Adv. Energy Mater.* **2014**, *4*, 1301453.
- [21] N. Yabuuchi, R. Hara, K. Kubota, J. Paulsen, S. Kumakura, S. Komaba, *J. Mater. Chem. A* **2014**, *2*, 16851.
- [22] U. Maitra, R. A. House, J. W. Somerville, N. Tapia-Ruiz, J. G. Lozano, N. Guerrini, R. Hao, K. Luo, L. Jin, M. A. Pérez-Osorio, F. Massel, D. M. Pickup, S. Ramos, X. Lu, D. E. McNally, A. V. Chadwick, F. Giustino, T. Schmitt, L. C. Duda, M. R. Roberts, P. G. Bruce, *Nat. Chem.* **2018**, *10*, 288.
- [23] A. Konarov, J. H. Jo, J. U. Choi, Z. Bakenov, H. Yashiro, J. Kim, S. T. Myung, *Nano Energy* **2019**, *59*, 197.
- [24] H. J. Kim, A. Konarov, J. H. Jo, J. U. Choi, K. Ihm, H.-K. Lee, J. Kim, S.-T. Myung, *Adv. Energy Mater.* **2019**, *9*, 1901181.
- [25] Z. Lu, J. R. Dahn, *J. Electrochem. Soc.* **2001**, *148*, A1225.
- [26] J. H. Jo, J. U. Choi, A. Konarov, H. Yashiro, S. Yuan, L. Shi, Y.-K. Sun, S.-T. Myung, *Adv. Funct. Mater.* **2018**, *28*, 1705968.
- [27] N. Yabuuchi, K. Yoshii, S. T. Myung, I. Nakai, S. Komaba, *J. Am. Chem. Soc.* **2011**, *133*, 4404.
- [28] J. Heyd, G. E. Scuseria, M. Ernzerhof, *J. Chem. Phys.* **2003**, *118*, 8207.
- [29] A. Konarov, J. U. Choi, Z. Bakenov, S.-T. Myung, *J. Mater. Chem. A* **2018**, *6*, 8558.
- [30] T. Roisnel, J. Rodríguez-Carvajal, *FullProf Manual* **2002**, p. 139.
- [31] M. Ravel, B. Newville, *J. Synchrotron Radiat.* **2005**, *12*, 537.
- [32] D. Kresse, G. Joubert, *Phys. Rev. B* **1999**, *59*, 1758.
- [33] G. Kresse, J. Furthmüller, *Comput. Mater. Sci.* **1996**, *6*, 15.
- [34] G. Kresse, J. Furthmüller, *Phys. Rev. B* **1996**, *54*, 11169.
- [35] P. E. Blöchl, *Phys. Rev. B* **1994**, *50*, 17953.
- [36] A. Van der Ven, J. C. Thomas, Q. Xu, J. Bhattacharya, *Math. Comput. Simul.* **2010**, *80*, 1393.
- [37] J. P. Perdew, K. Burke, M. Ernzerhof, *Phys. Rev. Lett.* **1996**, *77*, 3865.